Effect of selective laser melting process parameters on microstructural and mechanical properties of TiC-NiCr cermet

Atefeh Aramian[a,b], Zohreh Sadeghian[a*], Seyed Mohammad Javad Razavi[b], Konda Gokuldoss Prashanth[c,d,e], Filippo Berto[b]

[a]*Department of Material Science and Engineering, Faculty of Engineering, Shahid Chamran University, Golestan Boulevard, 6135785311 Ahvaz, Iran*
[b]*Department of Mechanical and Industrial Engineering, Norwegian University of Science and Technology (NTNU), Richard Birkelans vei 2b, 7491 Trondheim, Norway*
[c] *Department of Mechanical and Industrial Engineering, Tallinn University of Technology, Ehitajate Tee 5, 19086, Tallinn, Estonia*
[d] *Erich Schmid Institute of Materials Science, Austrian Academy of Sciences, Jahnstraße 12, A-8700 Leoben, Austria*
[e] *CBCMT, School of Mechanical Engineering,Vellore Institute of Technology, Vellore 632 014, Tamil Nadu, India*
**Corresponding author: z.sadeghian@scu.ac.ir*

Abstract

TiC-NiCr cemented carbide cermet was in situ synthesized through selective laser melting (SLM) process using Ti, C, and $Ni_{80}Cr_{20}$ powder mixture. Feedstock powder was prepared using high energy milling for a total milling time of 15 hours. The effects of input energy density on the phase evolution and microstructure of SLM samples were investigated using X-ray diffractometery (XRD) and field emission scanning electron microscopy (FESEM) equipped with an energy dispersive spectrometer (EDS). The density of in situ fabricated cermets was measured using Archimedes' principle, and microhardness and fracture toughness of the samples were determined through Vickers hardness test. Increasing the input energy density from 138.7 to 378.2 Jmm^{-3} resulted in an increase in relative density from 93.07% to 97.49% of theoretical density. Moreover, the microhardness and fracture toughness of the manufactured cermets

increased to 1369.5 HV_1 and 25.96, respectively. Further increasing of the energy density caused a reduction in all properties.

Keywords:

Selective laser melting (SLM); in situ cermet; TiC-based cermet; fracture toughness

1. Introduction

Cemented carbides (cermets) belong to a group of engineering materials comprised of metal (ductile) and ceramic (hard and brittle) phases. Due to their high ductility and hardness, cermets have been developed for numerous industrial applications such as cutting tools, aerospace, oil and gas industries which require high hardness, toughness, and wear resistance [1-4].

The most common industrial ceramics used in cermets are tungsten carbide (WC) and titanium carbide (TiC). Although both of these phases possess high Young's moduli, hardness, wear resistance, chemical and thermal stability, TiC has received more attention in recent years due to its lower density (4.93 $g.cm^{-3}$) in comparison with WC (15.63 $g.cm^{-3}$) [5-7].

Different types of metals are used as binders in TiC-based cermets. It is generally accepted that good wettability between the ceramic particles and metal binder improves the density and mechanical properties of cermet samples. It has been reported that TiC shows good wettability with a variety of molten metals, including Ni, Cu, Al, Co, and Fe, as well as their alloys [8]. Among metallic binders, Nickel alloys have been more widely used as binders in TiC-based cermets, due to their good mechanical properties and wear and corrosion resistance at high temperatures [9].

In recent years, additive manufacturing (AM) has emerged as a set of production methods used to manufacture components through computer-aided design (CAD) [10]. According to type of

feedstock, AM techniques are classified into the 3 main categories of liquid-based, solid-based, and powder-based methods. Selective laser melting/sintering (SLM/SLS), as a powder-based AM method, with the potential to produce a variety of materials such as steels [11-13], nickel-based alloys [14,15], titanium alloys [16,17], and aluminum alloys [18,19], has been considered a promising fabrication method that will most likely initiate the next industrial revolution [20]. SLM process is capable of producing specimens with complex designs the production of which is challenging and costly through conventional methods such as casting, forging, powder metallurgy, and machining. The process parameters of SLM include laser power, layer thickness, hatch spacing, and scan speed. To investigate the effects of process parameters on the properties of the manufactured samples, all parameters are considered in equation (1) as input energy density (η):

$$\eta = \frac{P}{vhd} \tag{1}$$

where η is energy density (J.mm^{-3}), P is laser power (W), v is scanning speed (mm/s), h is scanning hatch spacing (μm), and d is layer thickness (μm).

In the present research, the effects of process parameters on in situ synthesis of TiC-NiCr cermet through SLM were investigated. For this purpose, a powder mixture consisting of elemental Ti and C, and NiCr alloy was prepared by milling. The effects of variation in SLM energy density on the microstructure, hardness, and fracture toughness of the cermets were studied.

2. Material and experiments:

Commercially available Ti (98.9%; spherical; ≤ 45 μm), amorphous C (99.95%; spherical; 2-12 μm), and $Ni_{80}Cr_{20}$ (near-spherical; ≈ 20 μm) were used as the initial powders for the production

of TiC-NiCr cermet. Powder preparation was conducted in two steps of milling. First, a mixture of Ti and C powder was milled using a high-speed mill (Retch, E max, Germany) at 350 rpm in isopropanol for 5 hours. Subsequently, the milled powder was mixed with NiCr powder to achieve a nominal composition of 60 wt.%TiC-40 wt%NiCr, and the mixture was further milled for 10 hours in isopropanol. Fig. 1 shows the scanning electron microscopy (SEM) micrographs of the initial powders and milled powder, and X-ray diffraction (XRD) pattern of the milled powder mixture.

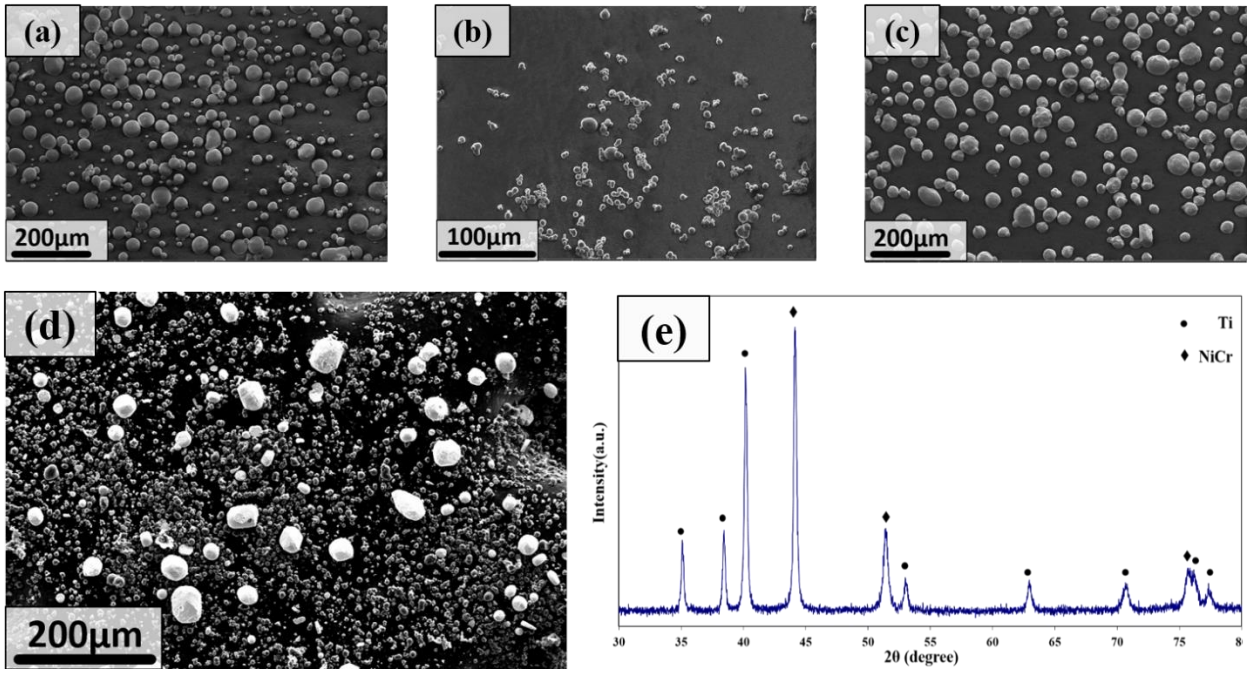

Fig. 1. SEM micrographs of a) Ti, b) C, c) NiCr powder, and (e) XRD pattern of the milled powder

The SLM process was performed using a Realizer SLM 50 system equipped with Nd:YAG fiber laser with a maximum power of 100 W. The SLM process parameters used in this research are presented in table 1.

Table 1. Selective laser melting process parameter

POWER (W)	HATCH SPACING (MM)	LAYER THICKNESS (MM)	SCAN SPEED ($MM.S^{-1}$)	ENERGY DENSITY ($J.MM^{-3}$)
62.4	60	50	150	138.7
			95	218.9
			60	346.7
			55	378.2
			50	416.0

The structural evolution of the milled powder and SLM samples was investigated using an X-ray diffractometer (D8 A25 DaVinci; Bruker Optics Inc., Billerica, MA, USA) with CuK_α radiation (λ = 0.15406 nm). XRD scans were performed between 30 and 85 degrees in 2θ with a step size of 0.02 degrees. Eva software (Bruker Optics Inc., Billerica, MA, USA) and Topas software (Bruker Optics Inc., Billerica, MA, USA) were used to analyze the XRD data. In order to study the morphology of powders and microstructure of SLM samples, field emission scanning electron microscopy (FESEM; Ultra 55 limited Edition; Zeiss, Oberkochen, Germany) equipped with an energy dispersive spectrometer (EDS) was used. Standard metallographic techniques of grinding and polishing were implemented, and final polishing was conducted with an ion polisher (IM-3000, Hitachi, Ltd., Chiyoda City, Tokyo, Japan) to prepare bulk samples for microstructural investigations.

The density of the SLM processed bulk samples was determined using Archimedes' principle. Vickers hardness of the SLM samples (cross-sectional and longitudinal) was determined using a microhardness testing machine (Zwick Roell Group, Ulm, Germany) under 1 kg loading with a dwell time of 10 seconds; the mean value of 5 measurements was reported for each sample. Fracture toughness of the samples was determined through the indentation method using 5 kgf

loading and 10 seconds dwell time; the mean value of 3 indentations on each sample was reported. The equation proposed by Shetty et al. [21] was used to measure the fracture toughness.

$$K_{IC} = \sqrt{\frac{\mathrm{HV}}{\sum_{i=1}^{i=4} l_i}} \tag{2}$$

Where K_{IC} is the fracture toughness, $\sum_{i=1}^{i=4} l_i$ is the sum of crack lengths of each indentation in mm, and HV is the hardness value in kgf.mm^{-2}.

3. Results and discussion

3.1. Phase identification

XRD patterns of TiC-NiCr cermets obtained through SLM with different scanning speeds are presented in Fig. 2. Sharp peaks related to the TiC phase, formed during the SLM process, can be seen in all XRD patterns. Other peaks of lower intensity related to NiCr binder and Ti-Ni intermetallic compound were also detected. At different input energy densities, the peaks corresponding to TiC were located at slightly higher than 2θ degrees compared to those of the stoichiometric compound, indicating the smaller lattice parameter of the produced TiC than that of the standard one (4.329 ˚A, PDF number 04-002-5189). Therefore, TiC can be considered a non-stoichiometric phase in the present study. The increase in lattice parameter due to increased input energy density can be attributed to a higher temperature as well as longer exposure time, which facilitates the diffusion of C into Ti lattice and the formation of near-stoichiometric TiC.

Energy density (Jmm^{-3})	138.7	218.9	346.7	378.2	416
Lattice parameter ($^{\circ}$A)	4.320	4.324	4.324	4.324	4.325

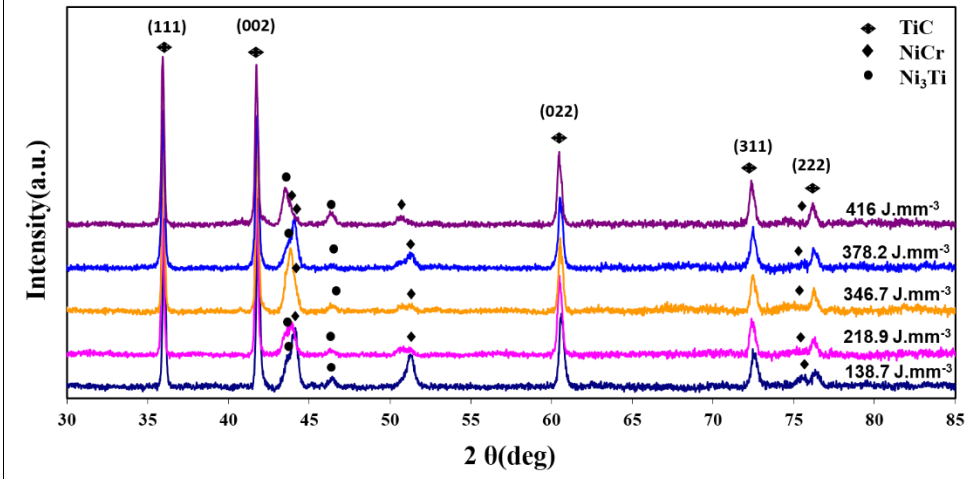

Fig2. XRD patterns of the samples manufactured with a) 138.7 J.mm^{-3}, b) 218.9 J.mm^{-3}, c) 346.7 J.mm^{-3}, d) 378.2 J.mm^{-3}, and e) 416 J.mm^{-3} energy densities

3.2. Microstructural characterization

SEM micrographs obtained from the transverse sections of the samples are presented in Fig. 3; two distinct zones of different sizes can be observed in the transverse sections of the SLM samples. A relatively fine structure can be mainly seen at the center of the laser hatches, surrounded by a coarser microstructure at the boundaries. In the longitudinal sections shown in Fig. 4, a gradient in the size of the TiC phase, with orientational growth from the center of the melt pool toward the boundaries, is noticeable. At the center of the melt pool, fine and equiaxed particles can be seen. A gradual increase in the size of the TiC phase and change in the morphology is observed from the center of the melt pool to its border. This can be explained by the temperature gradient from the center to the boundaries of the melt pool.

Due to the Gaussian distribution of laser energy, there is a temperature gradient (G) with maximum value at the center of the melt pool and minimum value at its boundaries. The grain

size changes gradually from the boundary to the center of the melt pool, which can be explained by the changes in fineness factor ($G \times R$) and shape factor (G/R) [22-25]. Moreover, the formation of coarse grains at the border of the melt pool has been explained by the re-melting of solidified materials during the scanning of the next hatch [26, 27]. However, Liu et al. [28] reported that the width of the coarse zone was smaller than the overlap between the two adjacent hatches [29]. The formation of the coarse zone can be related to the reheating of the material to the semi-solid state during the melting of the next layer or next hatch.

At higher scan speeds, more equiaxed fine grains were observed in the SEM micrographs. The formation of fine grain structure can be attributed to lower heat input in the melt pool that influences the solidification process. For a Gaussian distributed laser source, the maximum temperature of the melt pool is proportional to $P/\sqrt{v}$ ratio [30]:

$$T_{max} \alpha \frac{P}{\sqrt{v}} \quad (3)$$

where P is the laser power and v is the scanning speed.

At higher scan speeds, lower temperatures can be achieved in the melt pool, which means lower G, and consequently, smaller G/R. The smaller the G/R ratio, the more equiaxed grains were formed. Moreover, at higher scan speeds (lower input energy densities), a narrower melt pool of shallower depth was formed.

In addition to the aforementioned phenomena, in the case of rising temperature with increase in the input energy, the exothermic in situ reaction between Ti and C with a high negative enthalpy of formation (-192.9 $KJmol^{-1}$) can initiate a self-propagating high-temperature synthesis (SHS) reaction from the center of the melt pool or hatch [31,32]. This *in situ* reaction not only

facilitates the melting/reaction, but can also change the temperature gradient in the melt pool [33]. Therefore, regular grain size and shape gradient may not be observed in some parts of the melt pools. It is worth mentioning that by increasing the energy density, finer TiC particles were attained at the center of the melt pool, which can be related to the increased nucleation of TiC due to the higher input energy. When the input energy is increased, the activation energy for in situ reaction can be easily provided at the center of the laser hatch, and nucleation of the new phase will be widely triggered. Furthermore, the melt pool, which is depicted by dash lines on the FESEM micrograph, broadened with increase in the energy density. It is clear that increasing the input energy results in the broadening of the melt pool, but in the present study, more intensive reaction waves can also be responsible for melt pool widening.

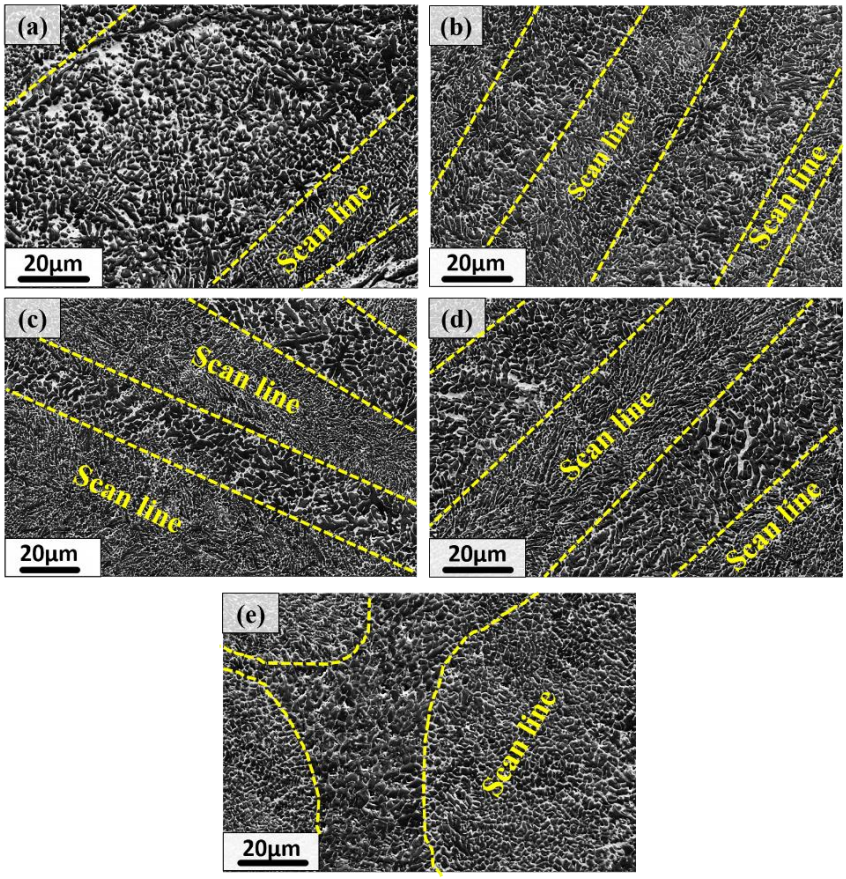

Fig3. SEM micrographs of the samples manufactured with, a) 138.7 J.mm^{-3}, b) 218.9 J.mm^{-3}, c) 346.7 J.mm^{-3}, d) 378.2 J.mm^{-3}, and e) 416 J.mm^{-3} energy densities

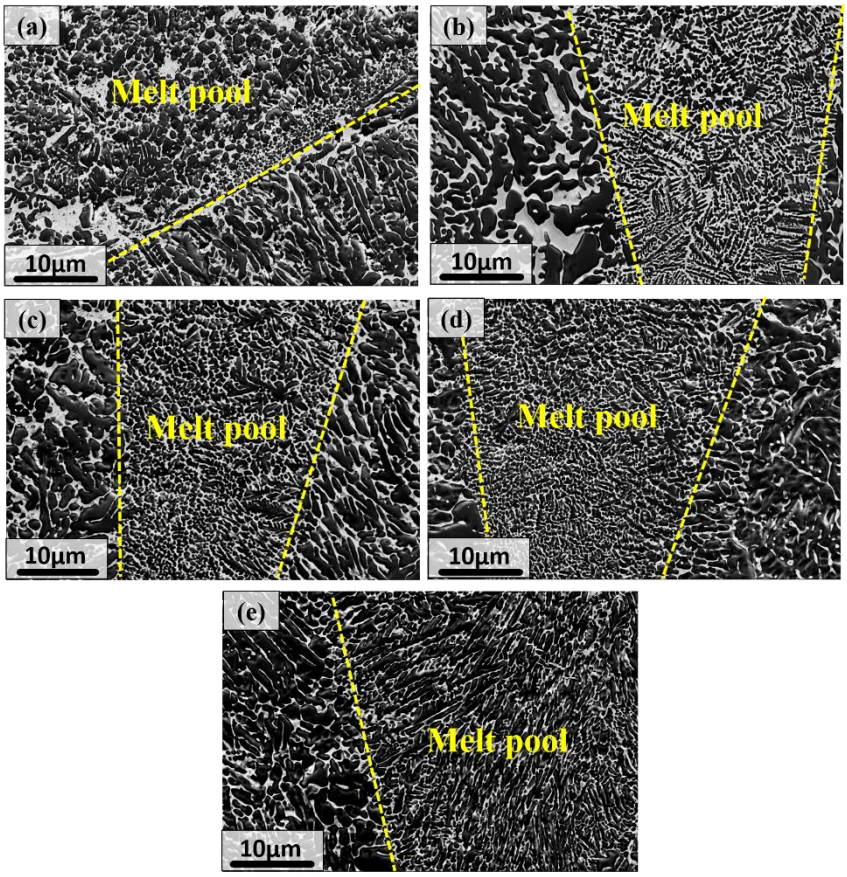

Fig. 4. SEM micrographs of the longitudinal section of the samples manufactured with a) 138.7 J.mm^{-3}, b) 218.9 J.mm^{-3}, c) 346.7 J.mm^{-3}, d) 378.2 J.mm^{-3}, and e) 416 J.mm^{-3} energy densities

Fig. 5 shows the EDS elemental maps of the vertical sections of the samples obtained from SLM with different energy densities. The distribution of Ti and C in the melt pool and at melt pool boundaries represents the distribution of TiC particles in different samples.

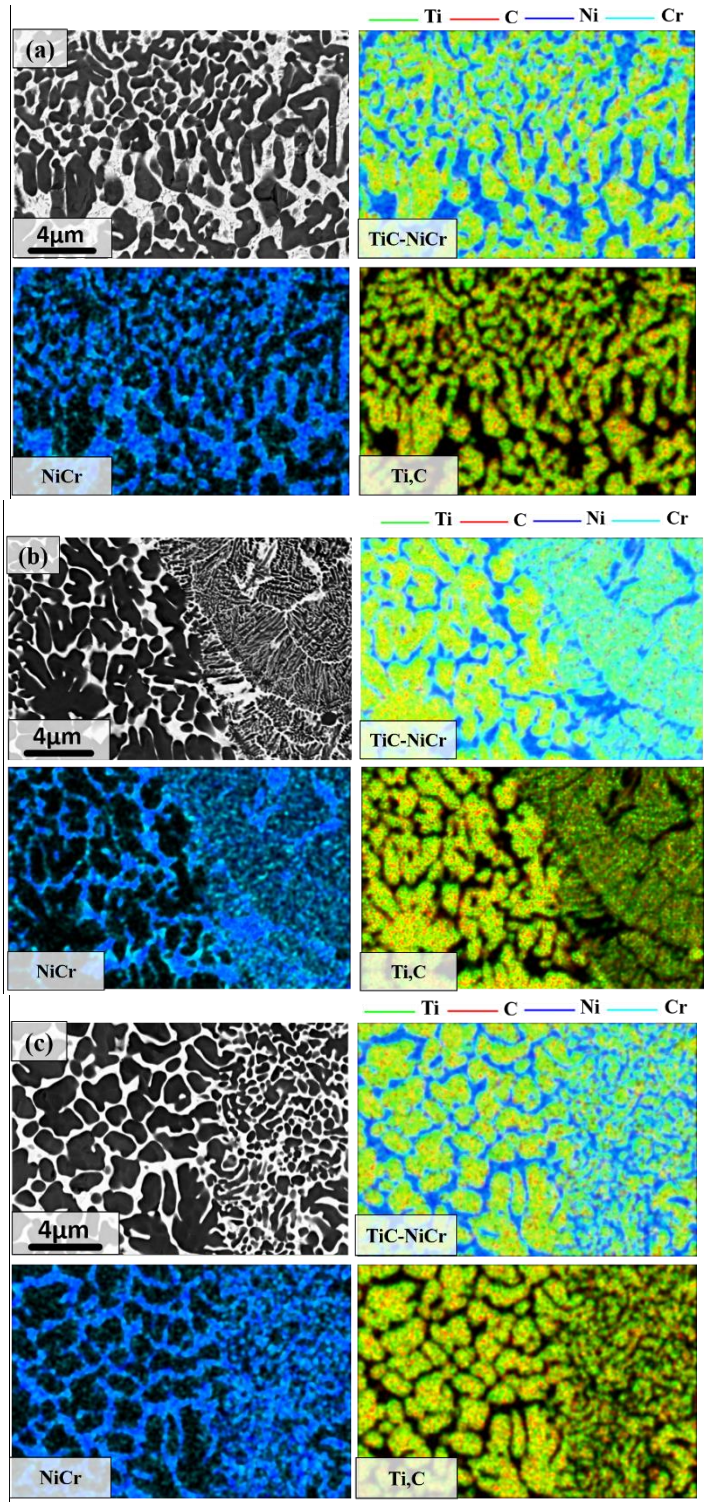
Ti
C
Ni
Cr
(a)
4μm
TiC-NiCr
NiCr
Ti,C
(b)
4μm
TiC-NiCr
NiCr
Ti,C
(c)
4μm
TiC-NiCr
NiCr
Ti,C

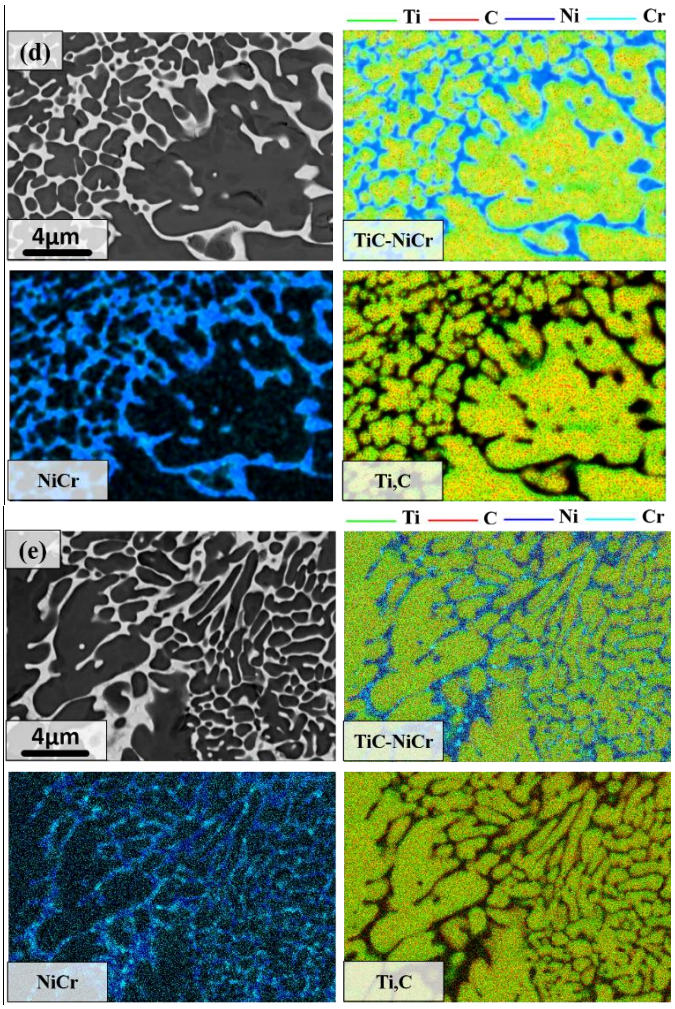

Fig. 5. EDS mapping of the samples manufactured with, a) 138.7 J.mm^{-3}, b) 218.9 J.mm^{-3}, c) 346.7 J.mm^{-3}, d)378.2 J.mm^{-3}, and e) 416 J.mm^{-3} energy densities

3.3. Density

The measured relative densities of the samples obtained with different energy densities are presented in table 2. Moreover, the volume percentage of porosities based on porosity values, and optical micrographs showing the porosities in the vertical section of the samples are presented in Fig. 6. At the minimum energy density of 138.7 J.mm^{-3}, the relative density of 93.07% was measured which increased to 97.49% with the increasing of energy density to 378.2 J.mm^{-3}. With energy densities of higher than 378.2 J.mm^{-3} (at 416 J.mm^{-3}), the relative density of

the sample decreased. At high scan speeds (low input energy densities), insufficient melting and instability of the melt flow can result in non-uniform distribution of the binder between TiC particles. Moreover, rapid heating and cooling may cause thermal stresses that induce crack formation. At lower scan speeds (increasing the input energy density), the laser exposure time increases and more thermal energy is released as a result of an exothermic reaction between Ti and C. Increasing the temperature of the melt pool results in decreased viscosity of the melt. Consequently, a more uniform distribution of the liquid between TiC particles will be attained. However, some microcracks and porosities were observed in the samples, which might have been formed due to liquid shrinkage or the difference in thermal expansion coefficient of ceramic and metal binder at the interface of the two phases. Further increasing of the energy density to 416 $J.mm^{-3}$ resulted in reduced density. Although it has been stated that high input energy densities can cause a reduction in viscosity, and thus, result in better consolidation, the coarsening of the in situ particles can increase the balling effect [30]. Moreover, evaporation is more likely to occur at high energy densities [34]. These two effects can be responsible for increased porosities in the manufactured samples. The volume percentage of porosity in the sample manufactured with low energy density (6.93%) was about 2.5 times higher than that of the sample produced with the highest density (2.51%).

Table 2. Density and porosity values obtained using Archimedes' principle

Energy Density ($J.mm^{-3}$)	Density ($gr.cm^{-3}$)	π_t (Vol%)	Relative Density (%)
138.7	5.25	6.93	93.07
218.9	5.37	4.99	95.01
346.7	5.44	3.65	96.35
378.2	5.51	2.51	97.49
416	5.38	4.67	95.27

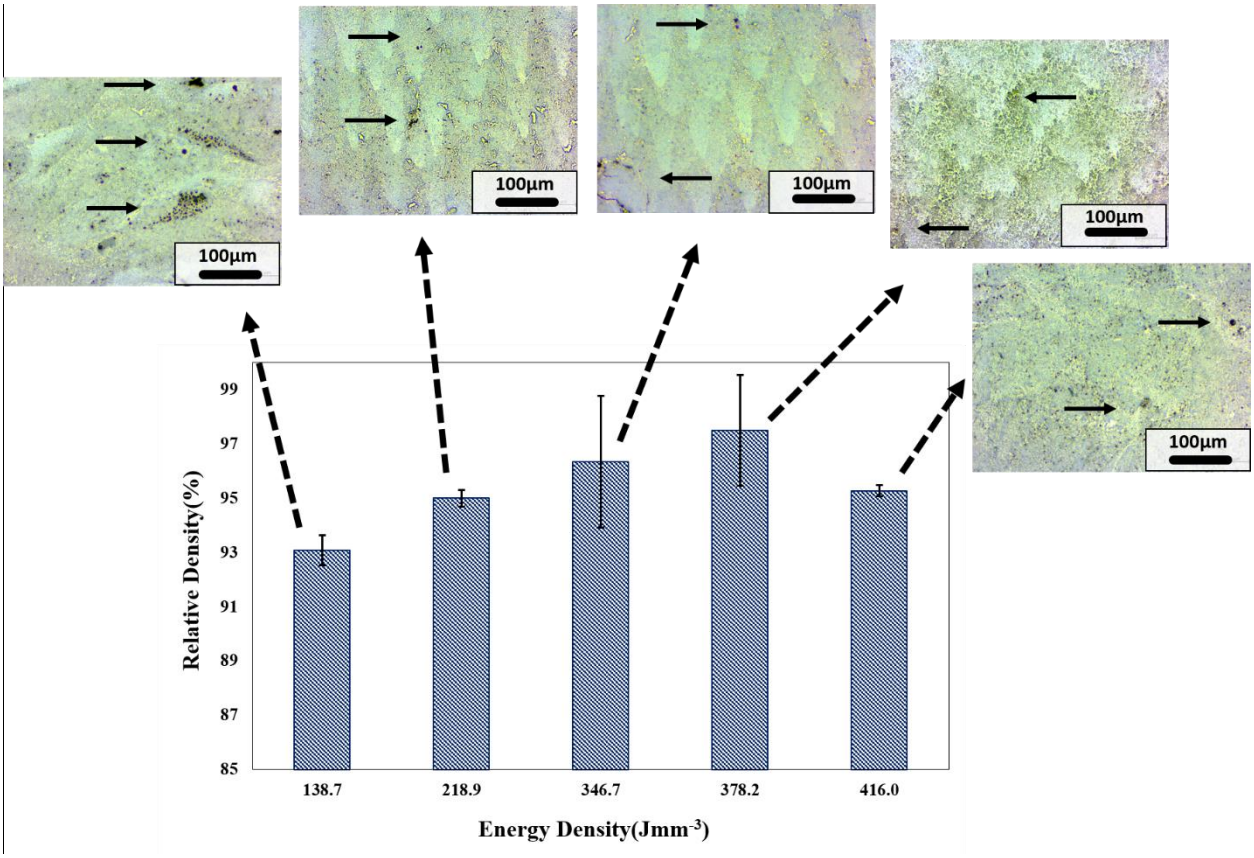

Fig. 6. Variation of relative density obtained using SLM with different energy densities

3.4. Process defects

The analysis of the cross sectional area of samples revealed a variety of porosities and defects as shown in Fig. 7. Different types of defects caused by (i) low energy density, (ii) the keyhole effect, (iii) entrapped gas, and (iv) the spattering effect could be detected in the manufactured samples.

At lower input energy densities, insufficient melting can be the possible reason for porosity formation (Fig. 7a). Xi et al. [35] reported that in some areas, the powder might embank because of inhomogeneous powder distribution, and therefore, at low energy densities, it may not melt entirely. They also stated that the melt pool around the mounded area is formed at a higher height than elsewhere. The keyhole effect has also been reported to form other kinds of voids as depicted in Fig. 7b. During the formation of the melt pool, some elements may evaporate, possibly resulting in the formation of a keyhole feature in the melt pool. The depth, size, shape, and probability of the formation of keyholes are affected by energy density, temperature distribution, and cooling rate that are considered process parameters [36,37].

The third kind of porosity is formed by entrapped gas (Fig. 7c) when the powder possesses a non-uniform morphology or a wide range of particle size distribution. As a result, the powder bed will not be completely covered, and the gas entrapped in inter-particle gaps forms gaseous bubbles of different sizes in the consolidated sample [38].

At high energy densities, the heat transfer from the melt pool to the boundaries may be inadequate, and this can cause overheating and evaporation of the melt. Vaporization may lead to the spattering of droplets as well as powder particles. As a result of the spattering of droplets, the volumes of materials in the molten pool decrease; consequently, voids are formed after solidification. These voids are filled with powder particles during the spreading of the next

powder layer so that the layer thickness increases locally in these areas. During the subsequent laser scanning, the melt pool that will be deeper at these zones may not reach the previously solidified layer. This can result in void formation as well as the presence of un-melted or partially melted particles in consolidated material. The spattered droplets may stick onto the powder bed in the scanning area, and large droplets can adhere to the powder bed and remain un-melted during the next laser scan. These droplets can act as obstacles to the streaming of the melt and cause void formation.

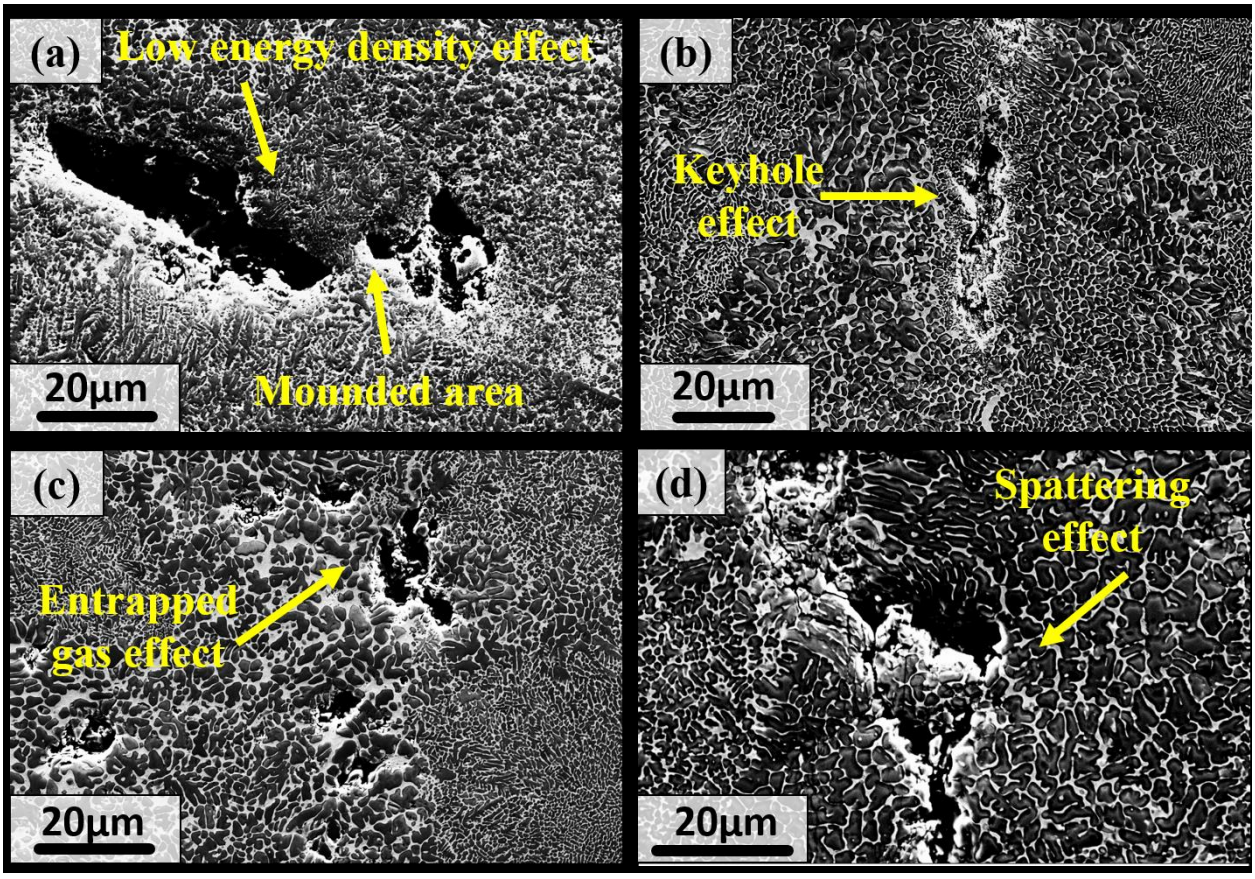

Fig. 7. Defects formed on the samples due to a) low energy density, b) the keyhole effect, c) entrapped gas, and d) the spattering effect

3.5. Hardness

Fig. 8 shows the mean microhardness values of the uppermost surface and cross section of the manufactured samples. The hardness of the samples increased with increase in energy density. The maximum hardness of 1370 HV was achieved at 378.2 J.mm^{-3} energy density, and as previously indicated the highest density with low rate of cracks and porosity was attained in this sample. Further increase in energy density resulted in reduced hardness that can be attributed to lower density, formation of cracks and porosity, and increased microstructural inhomogeneity and agglomeration of the in situ formed phase. Li et al. [39] manufactured in situ TiC-40 vol% Ni cermet using direct laser deposition and achieved a hardness value of about 1900 $HV_{0.3}$, while other researchers reported hardness values of about 1300 $HV_{0.5}$ and 1400 HV_1 in TiC based cermets [40,41].

The microhardness profiles of the longitudinal section of the samples show significant fluctuations at the lowest energy density, which can be explained by the inhomogeneous distribution of the TiC particles in the sample. With the increasing of the energy density up to 378.2 J.mm^{-3}, less variation was observed in the hardness values of different points in hardness profiles.

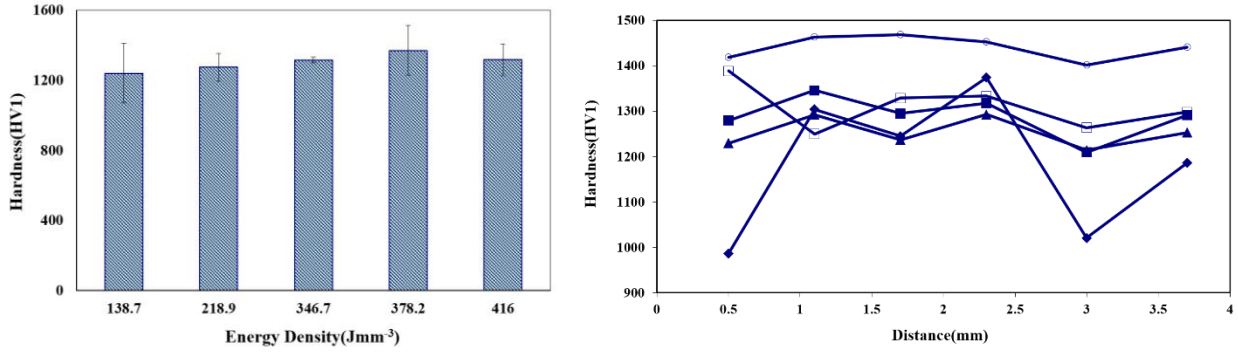

Fig. 8. Mean microhardness values a) of the uppermost surface, and b) along the longitudinal section of the samples produced using SLM process

3.6. Fracture Toughness

Fig. 9 shows the K_{IC} values of the samples manufactured at different energy densities. The results show an increase in fracture toughness with increase in energy density. The maximum value of fracture toughness measured in TiC-NiCr cermets was 25.9 $MPa.m^{1/2}$ in the sample obtained with the energy density of 378.2 $J.mm^{-3}$. This ascending trend can be explained by the higher relative density and more uniform distribution of the in situ particles in the binder obtained using higher energy densities. Gaier et al. [41] reported 19 $MPa.m^{1/2}$ fracture toughness in vacuum sintered TiC-30 wt.% Ni_3Al after heat treatment at 800˚C. As can be seen in Figs. 3 and 4, the particle size distribution in the coarse and fine zones has changed with increase in energy density. It has been shown in previous studies that dual size ceramic particles can result in higher fracture toughness. This has been attributed to bridging and the higher energy needed for crack propagation when cracks encounter larger particles [42]. The main mechanisms of the toughening of TiC-NiCr cermet seem to be crack deflection and intergranular and transgranular fracture as shown in Fig. 10. These mechanisms are activated by imposing high pressure which causes a considerable restraint force and ceramic particles hinder the crack propagation [43, 44]. Moreover, the in situ reaction leads to strong bonding at the ceramic/metal interface, which prevents the initiation and propagation of cracks at the interface [45]. It should be noted that by further increasing the energy density up to 416 $J.mm^{-3}$, a slight decrease occurred in fracture toughness, which can be related to the higher content of defects and porosities as shown previously.

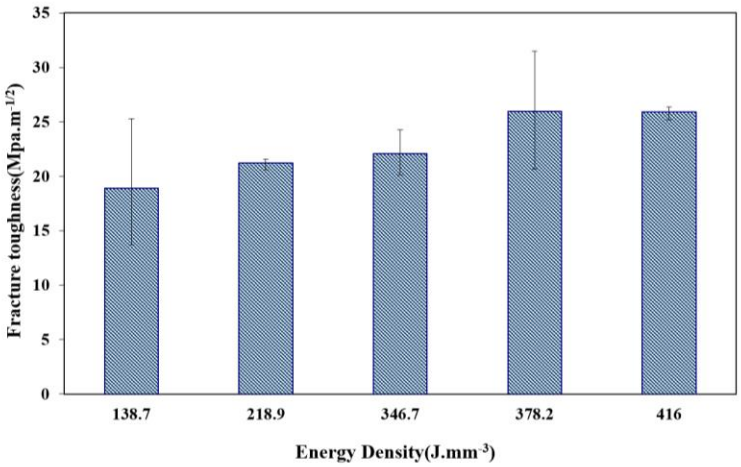

Fig. 9. Fracture toughness of the samples obtained using SLM process

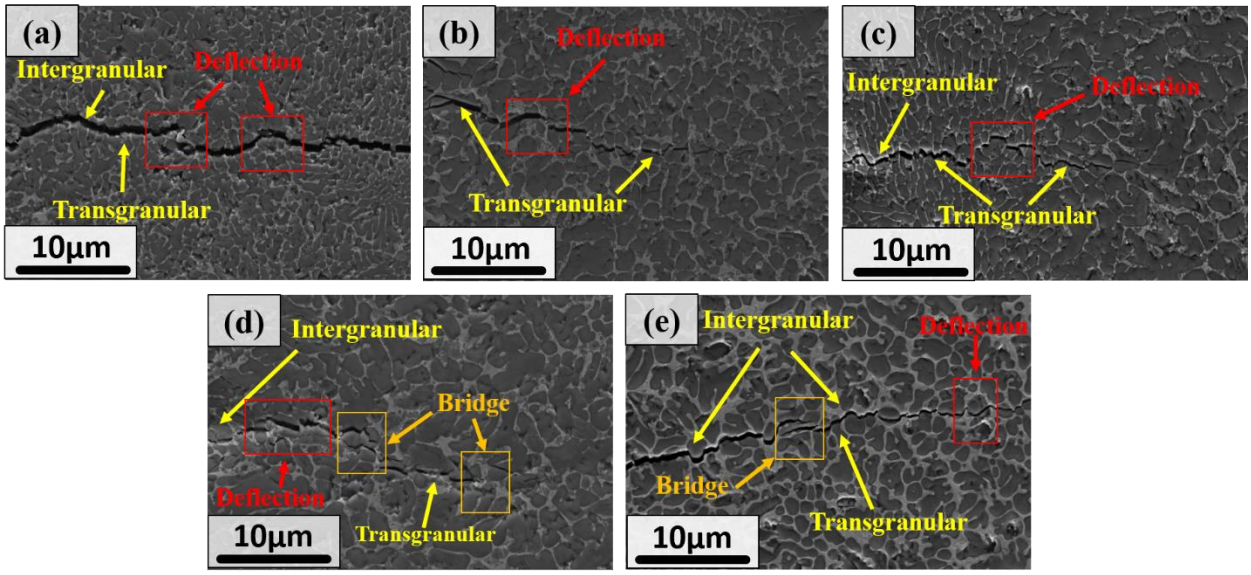

Fig. 10. SEM micrographs of crack propagation paths in TiC-NiCr samples fabricated at a) 138.7 J.mm^{-3}, b) 218.9 J.mm^{-3}, c) 346.7 J.mm^{-3}, d) 378.2 J.mm^{-3}, and e) 416 J.mm^{-3} input energy densities

Conclusion

In this study, the in situ TiC-NiCr cermet was successfully produced from Ti, C, and NiCr powder mixture using SLM process. Microstructural evolution, density, hardness, and fracture toughness of the manufactured samples were assessed.

Microstructural studies revealed two different grain size zones in the cross section of SLM samples. At the center of the melt pools, fine equiaxed TiC particles were formed. Moreover, a gradual increase in the size of the TiC phase and change in the morphology to a more dendritic structure was observed from the center of the melt pool to its border. The density of in situ manufactured samples increased with the increasing of the input energy density up to 378.2 $J.mm^{-3}$; however, further increasing of the input energy density up to 416 $J.mm^{-3}$ resulted in reduced density. Hardness and fracture toughness increased with the increasing of the energy density up to 378.2 $J.mm^{-3}$, but decreased at 416 $J.mm^{-3}$ due to the increment of defects and porosities.

Acknowledgement

The present research was supported by Shahid Chamran University of Ahvaz under grant number GN26247.

Data availability statement

The raw/processed data required to reproduce these findings cannot be shared at this time as the data is part of an ongoing study; however, raw data will be available on request.

References:

[1] Y. Peng, H. Miao, Z. Peng, Development of TiCN-based cermets: Mechanical properties and wear mechanism, Int. J. Refract. Met. Hard Mater. 39 (2013) 78–89. doi:10.1016/j.ijrmhm.2012.07.001.

[2] Z. Guo, J. Xiong, M. Yang, C. Jiang, WC-TiC-Ni cemented carbide with enhanced

properties, J. Alloys Compd. 465 (2008) 157–162. doi:10.1016/j.jallcom.2007.10.132.

[3] S. Buchholz, Z.N. Farhat, G.J. Kipouros, K.P. Plucknett, The reciprocating wear behaviour of TiC-Ni 3 Al cermets, Int. J. Refract. Met. Hard Mater. 33 (2012) 44–52. doi:10.1016/j.ijrmhm.2012.02.008.

[4] I.A. Ibrahim, F.A. Mohamed, E.J. Lavernia, Particulate reinforced metal matrix composites - a review, J. Mater. Sci. 26 (1991) 1137–1156. doi:10.1007/BF00544448.

[5] T.L. Stewart, K.P. Plucknett, The sliding wear of TiC and Ti(C,N) cermets prepared with a stoichiometric Ni3Al binder, Wear. 318 (2014) 153–167. doi:10.1016/j.wear.2014.06.025.

[6] A. Rajabi, M.J. Ghazali, J. Syarif, A.R. Daud, Development and application of tool wear: A review of the characterization of TiC-based cermets with different binders, Chem. Eng. J. 255 (2014) 445–452. doi:10.1016/j.cej.2014.06.078.

[7] T.L. Stewart, K.P. Plucknett, The effects of Mo2C additions on the microstructure and sliding wear of TiC0.3N0.7-Ni3Al cermets, Int. J. Refract. Met. Hard Mater. 50 (2015) 227–239. doi:10.1016/j.ijrmhm.2015.01.013.

[8] S. V. Dudiy, B.I. Lundqvist, Wetting of TiC and TiN by metals, Phys. Rev. B - Condens. Matter Mater. Phys. 69 (2004) 125421. doi:10.1103/PhysRevB.69.125421.

[9] J.K.N. Murthy, S. Bysakh, K. Gopinath, B. Venkataraman, Microstructure dependent erosion in Cr3C2-20(NiCr) coating deposited by a detonation gun, Surf. Coatings Technol. 202 (2007) 1–12. doi:10.1016/j.surfcoat.2007.03.017.

[10] E. Herderick, Additive manufacturing of metals: A review, in: Mater. Sci. Technol. Conf. Exhib. 2011, MS T'11, 2011: pp. 1413–1425.

[11] K. Kempen, E. Yasa, L. Thijs, J.P. Kruth, J. Van Humbeeck, Microstructure and

mechanical properties of selective laser melted 18Ni-300 steel, Phys. Procedia. 12 (2011) 255–263. doi:10.1016/j.phpro.2011.03.033.

[12] Z. Sun, X. Tan, S.B. Tor, W.Y. Yeong, Selective laser melting of stainless steel 316L with low porosity and high build rates, Mater. Des. 104 (2016) 197–204. doi:10.1016/j.matdes.2016.05.035.

[13] H. Gu, H. Gong, D. Pal, K. Rafi, T. Starr, B. Stucker, Influences of energy density on porosity and microstructure of selective laser melted 17-4PH stainless steel, in: 24th Int. SFF Symp. - An Addit. Manuf. Conf. SFF 2013, 2013: pp. 474–489.

[14] G.P. Dinda, A.K. Dasgupta, J. Mazumder, Texture control during laser deposition of nickel-based superalloy, Scr. Mater. 67 (2012) 503–306. doi:10.1016/j.scriptamat.2012.06.014.

[15] H. Helmer, A. Bauereiß, R.F. Singer, C. Körner, Grain structure evolution in Inconel 718 during selective electron beam melting, Mater. Sci. Eng. A. 668 (2016) 180–187. doi:10.1016/j.msea.2016.05.046.

[16] L. Thijs, F. Verhaeghe, T. Craeghs, J. Van Humbeeck, J.P. Kruth, A study of the microstructural evolution during selective laser melting of Ti-6Al-4V, Acta Mater. 58 (2010) 3303–3312. doi:10.1016/j.actamat.2010.02.004.

[17] B. Vrancken, L. Thijs, J.P. Kruth, J. Van Humbeeck, Microstructure and mechanical properties of a novel β titanium metallic composite by selective laser melting, Acta Mater. 68 (2014) 150–158. doi:10.1016/j.actamat.2014.01.018.

[18] T. Kimura, T. Nakamoto, Microstructures and mechanical properties of A356 (AlSi7Mg0.3) aluminum alloy fabricated by selective laser melting, Mater. Des. 89 (2016) 1294–1301. doi:10.1016/j.matdes.2015.10.065.

[19] T. Kimura, T. Nakamoto, M. Mizuno, H. Araki, Effect of silicon content on densification, mechanical and thermal properties of Al-xSi binary alloys fabricated using selective laser melting, Mater. Sci. Eng. A. 682 (2017) 593–602. doi:10.1016/j.msea.2016.11.059.

[20] B. Berman, 3-D printing: The new industrial revolution, Bus. Horiz. 55 (2012) 155–162. doi:10.1016/j.bushor.2011.11.003.

[21] W.D. Schubert, H. Neumeister, G. Kinger, B. Lux, Hardness to toughness relationship of fine-grained WC-Co hardmetals, Int. J. Refract. Met. Hard Mater. 16 (1998) 133–142. doi:10.1016/S0263-4368(98)00028-6.

[22] W. Li, S. Li, J. Liu, A. Zhang, Y. Zhou, Q. Wei, C. Yan, Y. Shi, Effect of heat treatment on AlSi10Mg alloy fabricated by selective laser melting: Microstructure evolution, mechanical properties and fracture mechanism, Mater. Sci. Eng. A. 663 (2016) 116–125. doi:10.1016/j.msea.2016.03.088.

[23] L. Thijs, K. Kempen, J.P. Kruth, J. Van Humbeeck, Fine-structured aluminium products with controllable texture by selective laser melting of pre-alloyed AlSi10Mg powder, Acta Mater. 61 (2013) 1809–1819. doi:10.1016/j.actamat.2012.11.052.

[24] F. Trevisan, F. Calignano, M. Lorusso, J. Pakkanen, A. Aversa, E.P. Ambrosio, M. Lombardi, P. Fino, D. Manfredi, On the selective laser melting (SLM) of the AlSi10Mg alloy: Process, microstructure, and mechanical properties, Materials (Basel). 10 (2017) 76. doi:10.3390/ma10010076.

[25] C. Yan, L. Hao, A. Hussein, P. Young, J. Huang, W. Zhu, Microstructure and mechanical properties of aluminium alloy cellular lattice structures manufactured by direct metal laser sintering, Mater. Sci. Eng. A. 628 (2015) 238–246. doi:10.1016/j.msea.2015.01.063.

[26] P. Wei, Z. Wei, Z. Chen, J. Du, Y. He, J. Li, Y. Zhou, The AlSi10Mg samples produced

by selective laser melting: single track, densification, microstructure and mechanical behavior, Appl. Surf. Sci. 408 (2017) 38–50. doi:10.1016/j.apsusc.2017.02.215.

[27] J. Zou, Y. Zhu, M. Pan, T. Xie, X. Chen, H. Yang, A study on cavitation erosion behavior of AlSi10Mg fabricated by selective laser melting (SLM), Wear. 376–377 (2017) 496–506. doi:10.1016/j.wear.2016.11.031.

[28] X. Liu, C. Zhao, X. Zhou, Z. Shen, W. Liu, Microstructure of selective laser melted AlSi10Mg alloy, Mater. Des. 168 (2019) 107677. doi:10.1016/j.matdes.2019.107677.

[29] S. Nafisi, D. Emadi, M.T. Shehata, R. Ghomashchi, Effects of electromagnetic stirring and superheat on the microstructural characteristics of Al-Si-Fe alloy, Mater. Sci. Eng. A. 432 (2006) 71–83. doi:10.1016/j.msea.2006.05.076.

[30] S. Cao, Z. Chen, C.V.S. Lim, K. Yang, Q. Jia, T. Jarvis, D. Tomus, X. Wu, Defect, Microstructure, and Mechanical Property of Ti-6Al-4V Alloy Fabricated by High-Power Selective Laser Melting, Jom. 69 (2017) 2684–2692. doi:10.1007/s11837-017-2581-6.

[31] S. V. Meschel, O.J. Kleppa, Standard enthalpies of formation of some 3d transition metal carbides by high temperature reaction calorimetry, J. Alloys Compd. 257 (1997) 227–233. doi:10.1016/S0925-8388(97)00023-6.

[32] A.K. Chaubey, K.G. Prashnath, N. Ray, Z. Wang, Study on in-situ synthesis of AL-TiC composite by self propagating high temperature synthesis process, Mater. Sci. An Indian J. 12 (2015) 454–461.

[33] S. Dadbakhsh, R. Mertens, L. Hao, J. Van Humbeeck, J.P. Kruth, Selective Laser Melting to Manufacture “In Situ” Metal Matrix Composites: A Review, Adv. Eng. Mater. 21 (2019) 1–18. doi:10.1002/adem.201801244.

[34] J.-P. Kruth, S. Dadbakhsh, B. Vrancken, K. Kempen, J. Vleugels, J. Van Humbeeck,

Additive Manufacturing of Metals via Selective Laser Melting: Process Aspects and Material Developments, in: Addit. Manuf., 2015: pp. 69–99. doi:10.1201/b19360-4.

[35] M. Xia, D. Gu, G. Yu, D. Dai, H. Chen, Q. Shi, Porosity evolution and its thermodynamic mechanism of randomly packed powder-bed during selective laser melting of Inconel 718 alloy, Int. J. Mach. Tools Manuf. 116 (2017) 96–106. doi:10.1016/j.ijmachtools.2017.01.005.

[36] Y.J. Liu, S.J. Li, H.L. Wang, W.T. Hou, Y.L. Hao, R. Yang, T.B. Sercombe, L.C. Zhang, Microstructure, defects and mechanical behavior of beta-type titanium porous structures manufactured by electron beam melting and selective laser melting, Acta Mater. 113 (2016) 56–67. doi:10.1016/j.actamat.2016.04.029.

[37] M. Courtois, M. Carin, P. Le Masson, S. Gaied, M. Balabane, A new approach to compute multi-reflections of laser beam in a keyhole for heat transfer and fluid flow modelling in laser welding, J. Phys. D. Appl. Phys. 46 (2013) 505305. doi:10.1088/0022-3727/46/50/505305.

[38] T. Vilaro, C. Colin, J.D. Bartout, As-fabricated and heat-treated microstructures of the Ti-6Al-4V alloy processed by selective laser melting, Metall. Mater. Trans. A Phys. Metall. Mater. Sci. 42 (2011) 3190–3199. doi:10.1007/s11661-011-0731-y.

[39] Y. Li, P. Bai, Y. Wang, J. Hu, Z. Guo, Effect of Ni contents on the microstructure and mechanical properties of TiC-Ni cermets obtained by direct laser fabrication, Int. J. Refract. Met. Hard Mater. 27 (2009) 552–555. doi:10.1016/j.ijrmhm.2008.07.006.

[40] C.K. Sahoo, M. Masanta, Microstructure and mechanical properties of TiC-Ni coating on AISI304 steel produced by TIG cladding process, J. Mater. Process. Technol. 240 (2017) 126–137. doi:10.1016/j.jmatprotec.2016.09.018.

[41] M. Gaier, T.Z. Todorova, Z. Russell, Z.N. Farhat, J.W. Zwanziger, K.P. Plucknett, The influence of intermetallic ordering on wear and indentation properties of TiC-Ni 3 Al cermets, Wear. 426–427 (2019) 390–400. doi:10.1016/j.wear.2018.12.034.

[42] G.J. Yang, P.H. Gao, C.X. Li, C.J. Li, Simultaneous strengthening and toughening effects in WC-(nanoWC-Co), Scr. Mater. 66 (2012) 777–780. doi:10.1016/j.scriptamat.2012.02.005.

[43] G. Zhao, C. Huang, H. Liu, B. Zou, H. Zhu, J. Wang, A study on in-situ synthesis of TiB2-SiC ceramic composites by reactive hot pressing, Ceram. Int. 40 (2014) 2305–2313. doi:10.1016/j.ceramint.2013.07.152.

[44] L. Wang, H. Liu, C. Huang, B. Zou, X. Liu, Effects of sintering processes on mechanical properties and microstructure of Ti(C,N)-TiB2-Ni composite ceramic cutting tool material, Ceram. Int. 40 (2014) 16513–16519. doi:10.1016/j.ceramint.2014.08.003.

[45] D. Vallauri, F.A. Deorsola, Synthesis of TiC-TiB2-Ni cermets by thermal explosion under pressure, Mater. Res. Bull. (2009). doi:10.1016/j.materresbull.2009.02.009.